Final Report

Hydrocarbon-Fueled Rocket Plume Measurement Using Polarized UV Raman Spectroscopy

To: Huu P. Trinh
TD61, Space Transportation Directorate
NASA Marshall Space Flight Center
Huntsville, AL 35812

From: Joseph A. Wehrmeyer
Mechanical Engineering Department
Vanderbilt University
Nashville, TN 37235

February 22, 2002

Table of Contents

Abstract

The influence of pressure upon the signal strength and polarization properties of UV Raman signals has been investigated experimentally up to pressures of 165 psia (11 atm). No significant influence of pressure upon the Raman scattering cross section or depolarization ratio of the N_2 Raman signal was found. The Raman scattering signal varied linearly with pressure for the 300 K N_2 samples examined, thus showing no enhancement of cross section with increasing pressure. However at the highest pressures associated with rocket engine combustion, there could be an increase in the Raman scattering cross section, based upon others' previous work at higher pressures than those examined in this work. The influence of pressure upon thick fused silica windows, used in the NASA Modular Combustion Test Article, was also investigated. No change in the transmission characteristics of the windows occurred as the pressure difference across the windows increased from 0 psig up to 150 psig. A calibration was performed on the UV Raman system at Vanderbilt University, which is similar to the one at the NASA-Marshall Test Stand 115. The results of this calibration are described in the form of temperature-dependent functions, f(T)'s, that account for the increase in Raman scattering cross section with an increase in temperarture and also account for the reduction in collected Raman signal if wavelength integration does not occur across the entire wavelength range of the Raman signal. These functions generally vary only by ~10% across their respective temperature ranges, except for the case of CO_2, where there is a factor of three difference in its f(T) from 300 K to 2500 K. However this trend for CO_2 is consistent with the experimental work of others, and is expected based on the low characteristic vibrational temperature of CO_2. A time-averaged temperature measurement technique has been developed, using the same equipment as for the work mentioned above, that is based upon high-spectral resolution UV Raman scattering. This technique can provide temperature measurements for flows where pressure cannot be measured.

Introduction

For several years, at NASA-Marshall's East Test Area at Test Stand 115, there has been an instrumentation trailer equipped with UV laser diagnostics equipment for use in analyzing mixing and combustion phenomena in high pressure test articles equipped with optical access. This equipment has been used in two measurement campaigns that qualitatively investigated the high pressure mixing and combustion performance of rocket engine injectors.

UV Laser Diagnostics for Swirled LOx/Gaseous H_2 Injectors

The first campaign utilized the "Unielement Test Article" to investigate the performance of swirled liquid O_2/gaseous H_2 injectors for high oxygen/fuel ratio applications (such as in oxidizer turbopump preburners for full flow staged combustion cycle engines) [Wehrmeyer et al. 1997, 2001a]. Figure 1 shows a schematic of the UV laser diagnostics system, parts of which are located inside the trailer or on the Test Stand 115 pad. In addition Fig. 1 shows the Unilement Test Article. Figure 2 shows a detailed schematic of the test article, pointing out the multiple optical access designed into it. Another feature of the test article is its ability to provide a "background gas" environment that simulates the effect of neighboring injectors upon just one injector's flowfield. Ultraviolet Raman spectroscopy was used to obtain the instantaneous light "snapshots" shown in Fig. 3. The spectra in Fig. 3 are for a 20 second, 6 MPa test using N_2 as the background gas.

UV Laser Diagnostics for LOx/Liquid Methane Injectors

A second measurement campaign, again using UV Raman spectroscopy, investigated the mixing performance of a candidate injector for a liquid methane-fueled Mars ascent engine design. For the application of UV Raman scattering to hydrocarbon-fueled flows a technique has been developed to remove the interfering polycyclic aromatic hydrocarbon fluorescence from the relatively weak Raman signals. This technique, developed at NASA-Marshall, takes advantage of the strongly polarized nature of Raman scattering [Wehrmeyer et al. 2000; Hartfield et al. 1997]. Ultraviolet Raman scattering signals have been shown to be discernable from unpolarized fluorescence interference by subtracting one polarized image from another. Both of these polarized images are obtained from a single laser pulse by using a polarization-separating calcite crystal mounted in an imaging spectrograph. Figure 4 shows the modification to the original UV Raman system that allows polarized UV Raman signals to be obtained. The modification is simply the insertion of the calcite crystal (approximately 8 mm x 16 mm by 36 mm) into the imaging spectrograph. This displaces light of one linear polarization from the other polarization. Figure 5 shows an example of the polarization-resolved UV Raman images that are obtained from such a system. In this figure, which is an instantaneous UV Raman image from humid room temperature air, the Raman signal that is the same polarization as the laser is very intense, from O_2, N_2, and H_2O, but the other polarization shows only an extremely weak signal, due to the highly polarized nature of Raman scattering.

The polarized UV Raman technique was applied to a high pressure (3 MPa) test of co-annular LOx/liquid methane injectors that were housed in the Modular Combustion Test Article (MCTA). This test article was developed in-house at NASA-Marshall and has several parts, or

modules, including an optical access module, an ignitor module, and an endplate module, and these modules can be stacked in a variety of configurations. Figure 6 shows a schematic of the MCTA. Several high pressure tests, approximately 10 sec in duration, were conducted using the polarized UV Raman technique. Figure 7 shows results from one of those tests. The two polarized Raman images are visible in each of the four instantaneous Raman images of Fig. 7. However, unlike Fig. 5, the Raman images in Fig. 7 show approximately equal signal strength for both polarizations. This unexpected situation prevented the successful use of the polarized UV Raman technique to this hydrocarbon combustion situation.

Motivation for Present Work

The two previous applications of UV Raman to high pressure test articles resulted in only qualitative information. The signal strength of the various UV Raman signals could only give information about the presence or absence of a particular gas species, and could not be used to quantitatively infer what the species concentrations were, nor the temperature. To allow quantitative data to be obtained, an experimental calibration of the technique needs to be accomplished. Additionally the unpolarized nature of the UV Raman signals at high pressure should be investigated. This is the motivation for the work described in this report.

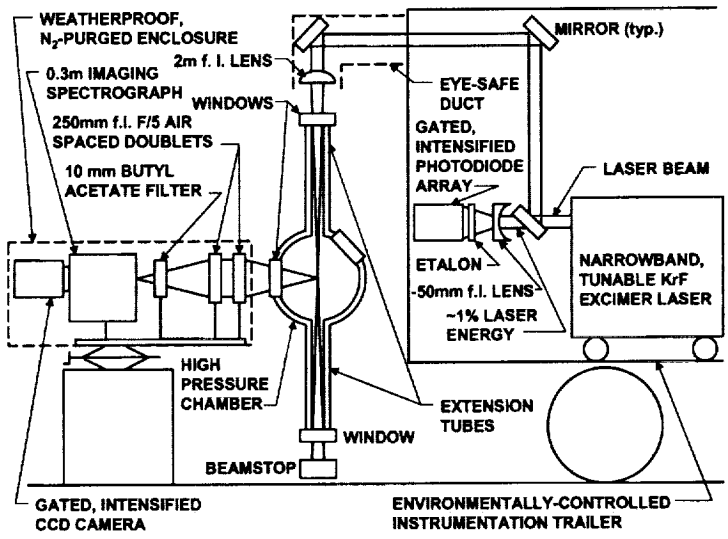

Fig. 1. Schematic of UV Raman system at Test Stand 115, along with Unielement Test Article.

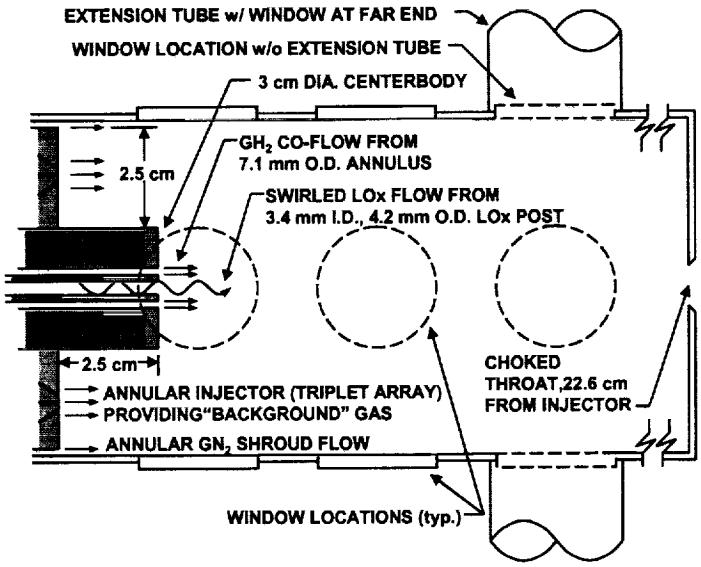

Fig. 2. Detailed schematic of the Unielement Test Article.

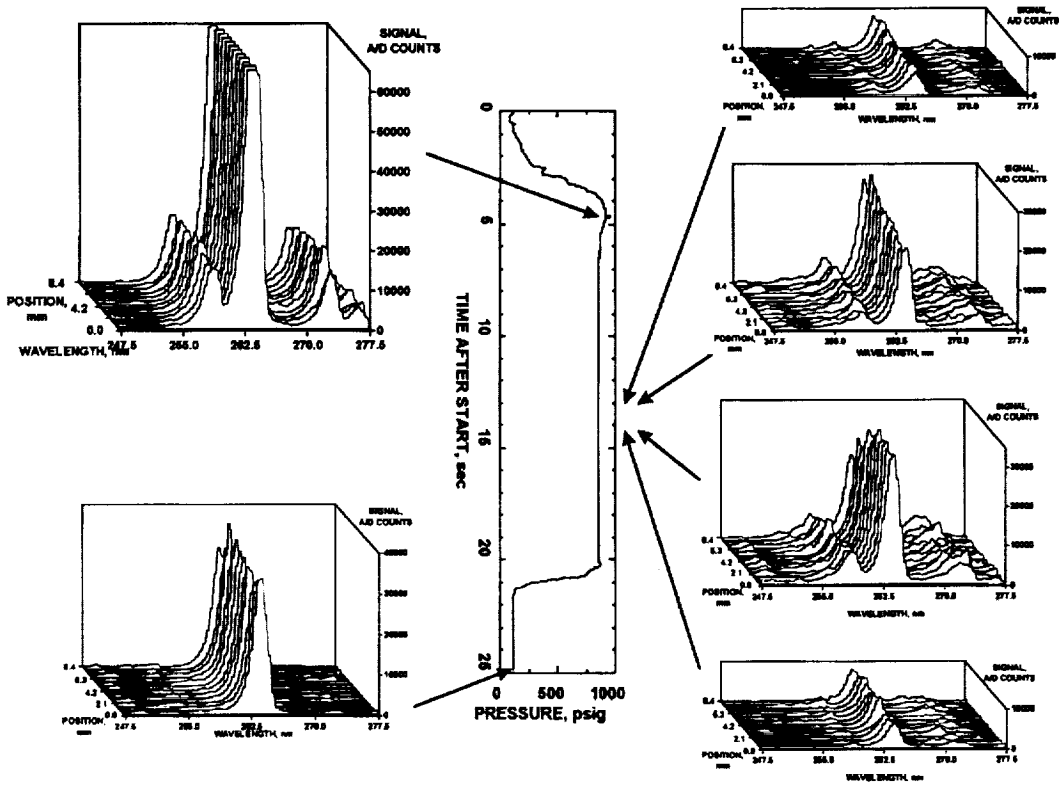

Fig. 3. Instananeous Raman images from Unielement Test Article with swirled coaxial injector with high O/F ratio LOx/gaseous H_2.

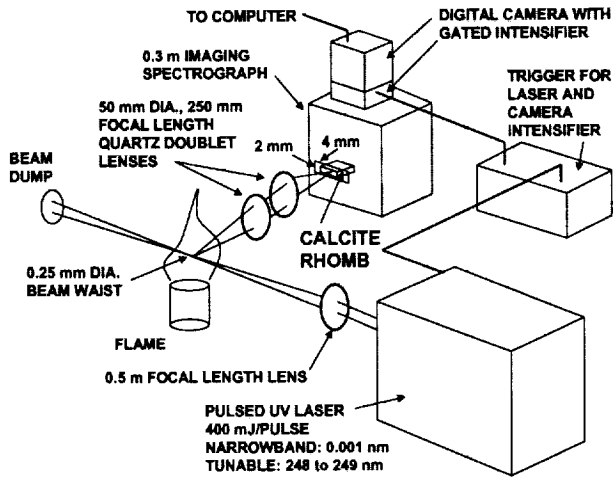

Fig. 4. Schematic of polarized UV Raman system showing insertion of calcite crystal into spectrograph.

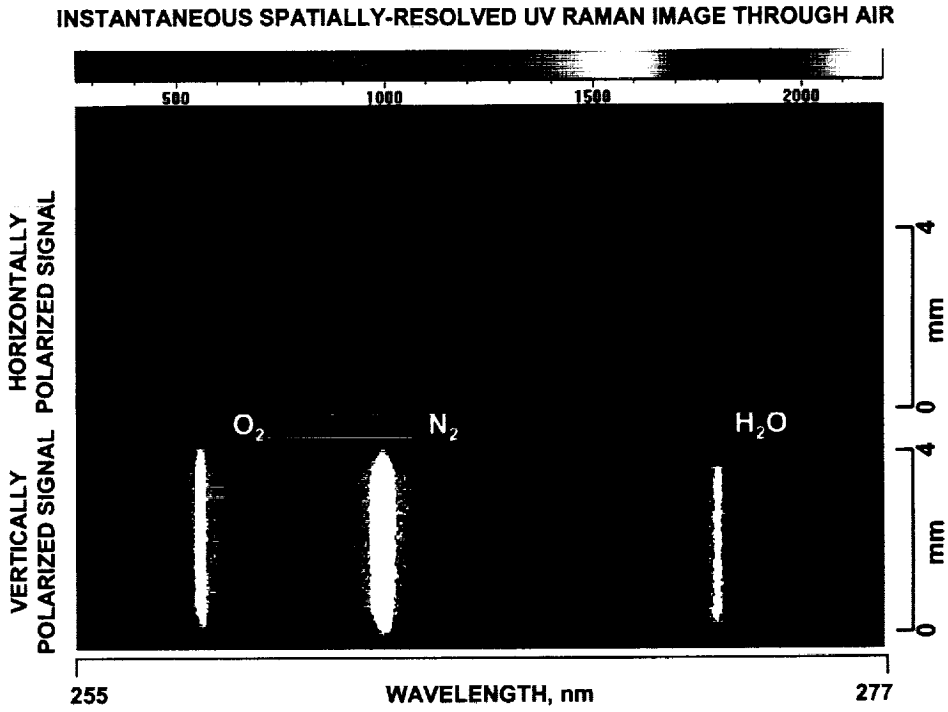

Fig. 5. Instantaneous, polarized UV Raman image of humid, room temperature air.

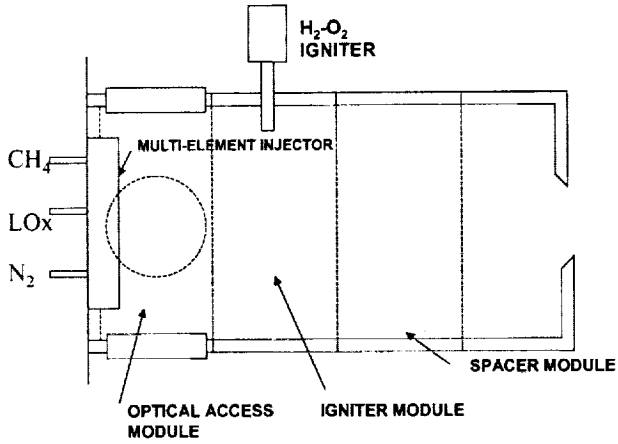

Fig. 6. Schematic of Modular Combustion Test Article.

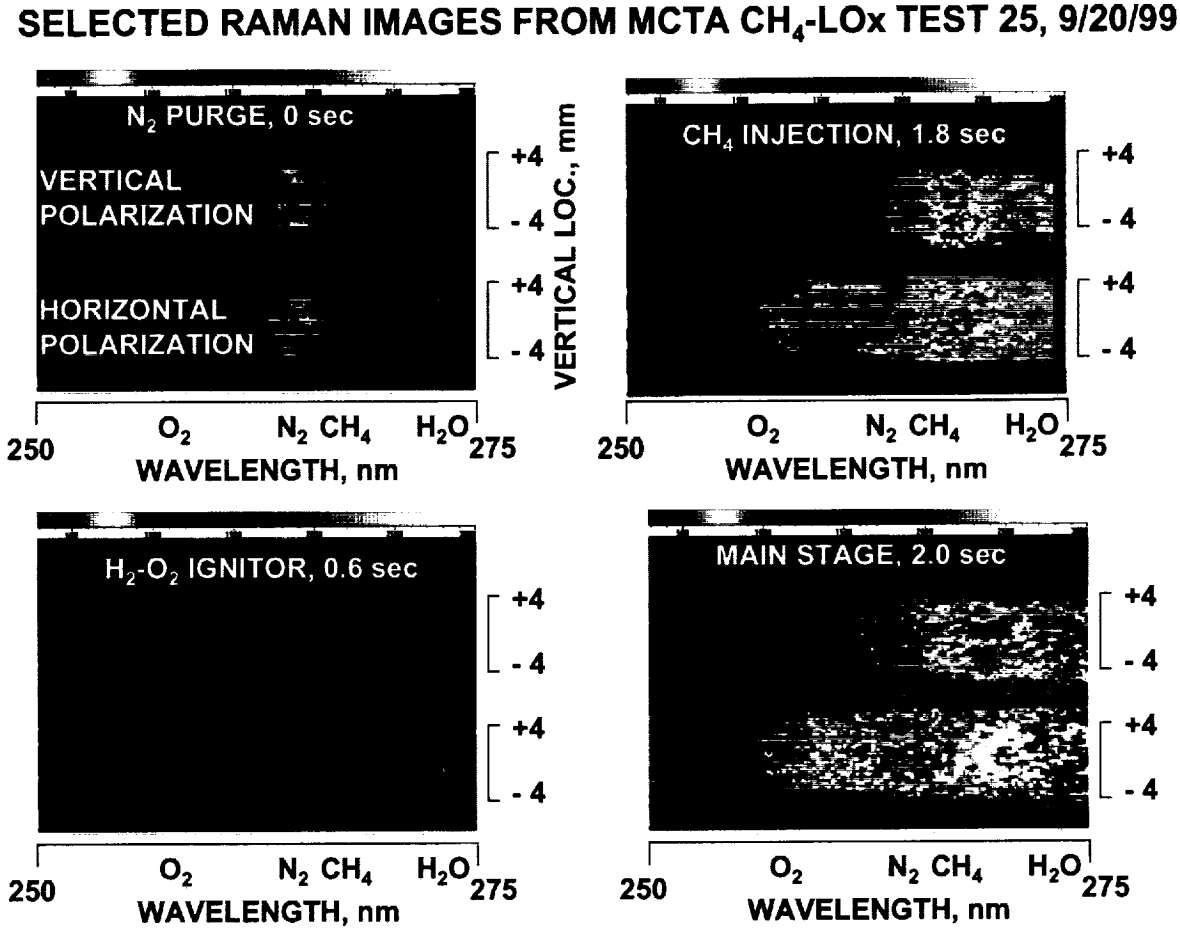

Fig. 7. Selected Raman images from early part of hot-fire test sequence for MCTA using multi-element liquid CH_4/LOx injector. Main stage pressure: 450 psig. Laser horizontally polarized.

High Pressure Effects

Background

The simplest working equation that can be used to relate the strength of a gas species Raman signal (N, where N is the number of Raman signal photons measured) to that signal's concentration (or number density, n) is given in Eq. 1. In this equation the strength of a single laser pulse, in terms of number of photons, is given by N_{laser}. The tendency for these laser photons to be consumed and re-emitted as Raman photons is given by the Raman scattering cross section σ. The fraction of Raman photons, emanating from one particular location down the path of the pulsed laser beam, that are collected and measured is given by the collection efficiency factor Ω. Lastly each location along the laser beam path scatters Raman photons, so N also depends upon the length of laser beam, L, along which Raman photons are collected and measured:

$$N = n \sigma N_{laser} \Omega L. \quad (1)$$

If it can be assumed that σ, N_{laser}, Ω, and L are all constant, then there is a simple linear relationship between N and n for each gas species. However σ is in general not a constant but depends upon temperature T, density ρ, and even the gas mixture that the scattering molecule exists in, which can be described by a set of mole fractions X_i for m different species. Hence:

$$\sigma = \sigma(T, \rho, X_1, X_2, \ldots, X_i, \ldots, X_m). \quad (2)$$

Reasons for the functional dependence of σ upon T are based upon the change in a molecule's polarizability as its structure is changed. A molecule at a higher T can be viewed as having a different structure than for a lower T, such as a longer internuclear separation distance from higher vibrational frequencies (at a high vibrational quantum number V) or from stronger centrifugal stretching (for a high rotational quantum number J). Increased scattering from increased ρ occurs due to increased intermolecular interactions at high ρ, and these depend upon the neighboring molecules of the scattering molecules, hence the dependence on X_i. The Raman scattering cross section also depends upon the polarization state of the laser as well as the assumed polarization state of the detected Raman photons. The amount of detected Raman photons that retain the polarization of the laser is often labeled as $N_{\parallel}$ and the Raman photons that have the orthogonal linear polarization are labeled as $N_{\perp}$. This is shown schematically in Fig. 8. The depolarization ratio is defined as the ratio of $N_{\perp}$ to $N_{\parallel}$ and is typically a small fraction, typically a value from 0.01 to 0.1. Figure 5 qualitatively shows the depolarization of room temperature, atmospheric pressure O_2, N_2, and H_2O. The $N_{\perp}$ to $N_{\parallel}$ ratio for O_2 is shown to be the highest in Fig. 5, along with H_2O shown to be the lowest. This is consistent with the findings of others [Lapp et al. 1973].

In considering the effect of pressure upon Raman scattering signals, one must consider the effect of pressure upon both the Raman signal strength and the signal's polarization. The study of molecular motion in dense fluids has included the application of Raman spectroscopy and as a result there have been some previous investigations into these phenomena [Wang and Wright 1973; Fabre and Oskengorn 1992]. These previous works have generally shown that σ

increases with an increase in ρ. For example, at the highest pressures expected in rocket engine test articles (~3000 psia, or ~200 atm) σ is expected to be ~25% greater than σ at 1 atm, for N_2, based on one investigation [Fabre and Oksengorn 1992]. However for other investigations at lower pressures no dependence of σ upon ρ was found; Gu et al. [2001] found a constant value of σ for N_2 and other species up to pressures of 60 bar for a temperature of 300K. Likewise Wang and Wright [1973] found an approximately constant value for σ for N_2 up to molar densities of 300 amagat (1 amagat is the molar density of a perfect gas at 1 atm and ~300 K).

An additional concern at high pressures, for the polarized UV Raman technique, is the effect that increased density has upon the depolarization ratio of a gas species Raman signal. Looking again at a previous work, it has been found that increased ρ has an effect on depolarization ratio. For N_2 the depolarization ratio decreases, as molar density increases from 1 to 400 amagat, while for CO the depolarization ratio increases [Wang and Wright 1973]. If there were a significant increase expected in the depolarization ratio at high ρ, then the polarized UV Raman technique would be problematic when applied at high pressure. While the results of Fig. 7 suggest a great increase in depolarization ratio for N_2 at high pressure, the opposite findings of Wang and Wright [1973] indicate that the effect of increased pressure (or ρ) upon the depolarization ratio of Raman signals needs to be further investigated.

Another aspect of depolarization of either the Raman signals or the laser beam is associated with the optical properties of the windows for a high pressure test article. Previous high pressure work [Wang and Wright 1973] has shown that quartz windows are less sensitive to stress-induced polarization effects than sapphire windows, although sapphire windows have been used for some recent high pressure studies [Fabre and Oksengorn 1992] in addition to quartz windows [Gu et al. 2001]. Fused silica quartz windows were used for the UV Raman work at NASA-Marshall. It was presumed that they did not affect the polarization state of either the laser beam or the Raman signals. However, based upon the results shown in Fig. 7, the polarization properties of the windows need determination.

Experimental: Effect of Pressure on Raman Signal Strength and Depolarization Ratio

An experimental system was constructed at Vanderbilt University that is similar to the UV Raman system at Test Stand 115. Figure 9 shows this system's schematic. Rather than a 0.3 m Acton imaging spectrograph, as is used at Test Stand 115, a Chromex 250is 0.25m imaging spectrograph is used, which has similar imaging capabilities. To provide polarization-resolved Raman signals, a calcite crystal was purchased. To determine the relative quality of this crystal compared to the NASA-Marshall crystal, each was inserted into a spectrophotometer (located at Belmont University) and their UV transmission characteristics were determined. Figure 10 shows the two transmission curves for the two crystals, and both curves are averages of both polarizations. The NASA-Marshall crystal, at all UV wavelengths, has significantly better light transmission than for the newer Vanderbilt crystal. However the Vanderbilt crystal represents the best quality crystal that can be obtained currently. The same vendor supplied both crystals (Karl Lambrecht Corporation) although the NASA crystal was supplied circa 1996 and the Vanderbilt crystal in 2000. Between those dates, according to the vendor, the world's supply of high purity natural calcite has greatly diminished, thus making the NASA crystal an extremely valuable item.

The schematic of Fig. 9, in addition to showing the Vanderbilt crystal and spectrograph, also shows a high pressure gas sample cell located in the laser beam path. This sample cell is constructed of a 1 inch outer diameter stainless steel tube, and at each end of the tube are fittings for small (1 inch dia.) fused silica windows to allow in and out of the sample cell a focused laser beam. At the middle of the 24 inch long tube is a three-way "T" fitting that allows a relatively large custom-made fitting to be inserted at 90 degrees to the tube axis. Figure 11 shows a schematic of this fitting, which was designed specifically to hold the fused silica windows of the NASA-Marshall Modular Combustion Test Article.

Due to safety concerns, the maximum pressure used in the Vanderbilt high pressure cell was 165 psia (11 atm or 1.1 MPa). This is significantly below the pressures of either of the two previous UV Raman tests at NASA-Marshall (6 MPa and 3 MPa), but still should be sufficient to determine if pressure affects either the Raman cross section or depolarization ratio.

Figure 12 shows Raman signal strength as a function of pressure for the N_2 Raman signal. Both polarizations are shown. There is essentially a linear relationship between Raman signal strength and pressure for the $N_{\parallel}$ polarization, which is the strongest of the two polarized signals. The $N_{\perp}$ polarized signal is slightly nonlinear with ρ, even at 165 psig. There is a slight reduction in the $N_{\perp}$ cross section with an increase in ρ. This has been explained by others [Wang and Wright 1973] as due to the fact that the $N_{\perp}$ scattering is caused by reorienting molecules (whose dipole moments have rotated between the times that a laser photon is absorbed and a Raman photon is emitted) and molecular collisions are more efficient at de-exciting these reorienting molecules than for de-exciting non-reorienting molecules that cause the $N_{\parallel}$ scattering. This is not the case for all molecules; for CO the same authors [Wang and Wright 1973] see the opposite effect. As a result of the slight decrease in the $N_{\perp}$ cross section with increasing pressure, there is a decrease in the depolarization ratio for N_2 with an increase in pressure, which is shown in Fig. 13.

Experimental: Effect of Pressure on Fused Silica Window Polarization Properties

In order to determine if the windows used on the Modular Combustion Test Article have any kind of polarization characteristics, either in the unstressed state or at high pressure, the following tests were performed. First N_2 Raman signals were obtained from the sample cell while no fused silica window was in the holder. Next one of the 1.5 inch thick windows were inserted into the specially made holder shown in Fig. 11. Another set of Raman signal measurements were obtained, again at normal atmospheric pressure. Finally a third set of Raman measurements were obtained through the window, but now with the window in a stressed state corresponding to the maximum pressure safely obtainable in the pressure cell (11 atm). For all three sets of measurements there was no difference in the depolarization ratio, indicating that the window, from pressures of 0 atm gage up to 10 atm gage, has no effect on the polarization properties of the measured Raman signals.

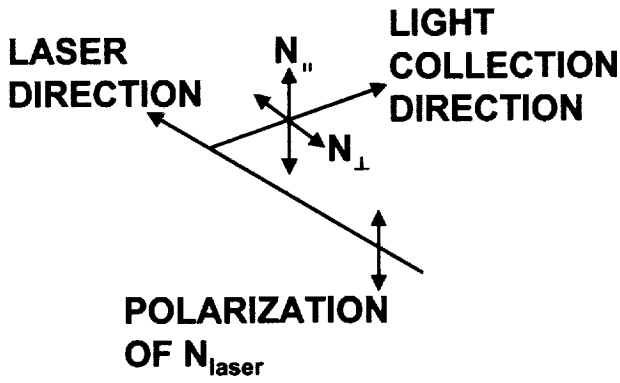

Fig. 8. Schematic showing definitions of $N_{\parallel}$ and $N_{\perp}$ polarization states.

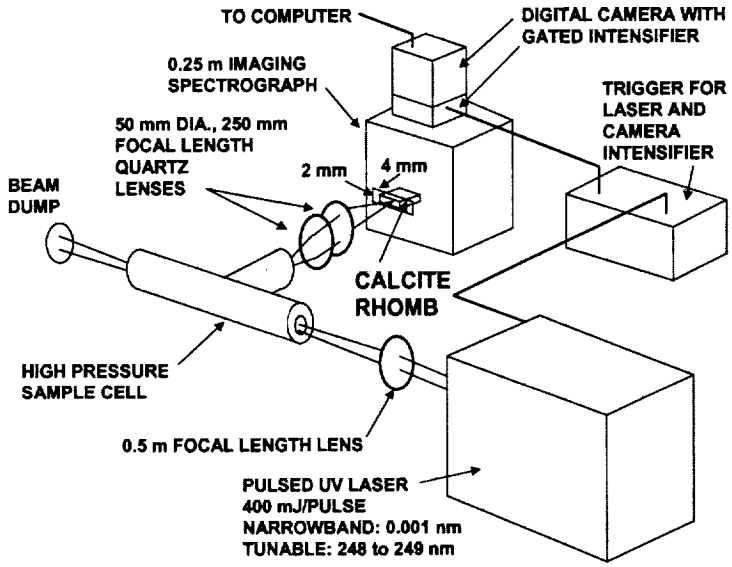

Fig. 9. Schematic of Vanderbilt polarized UV Raman system showing high pressure gas sample cell.

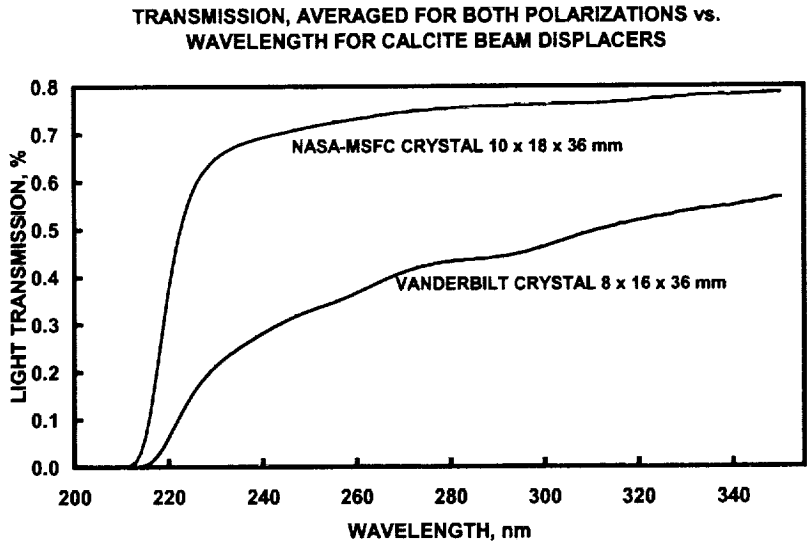

Fig. 10. Ultraviolet transmission characteristics of the NASA-Marshall and Vanderbilt polarization separation calcite crystals.

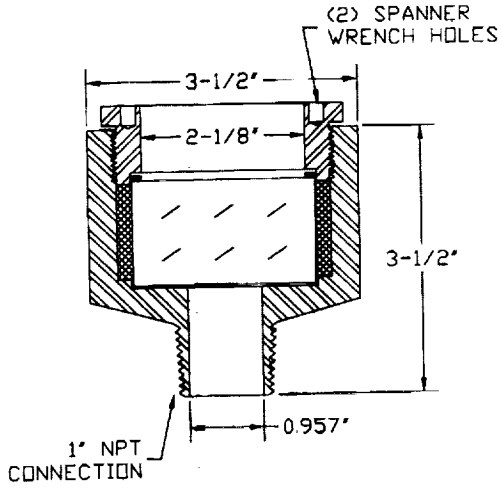

Fig. 11. Fitting for NASA-Marshall MCTA windows to mount in Vanderbilt high pressure gas cell.

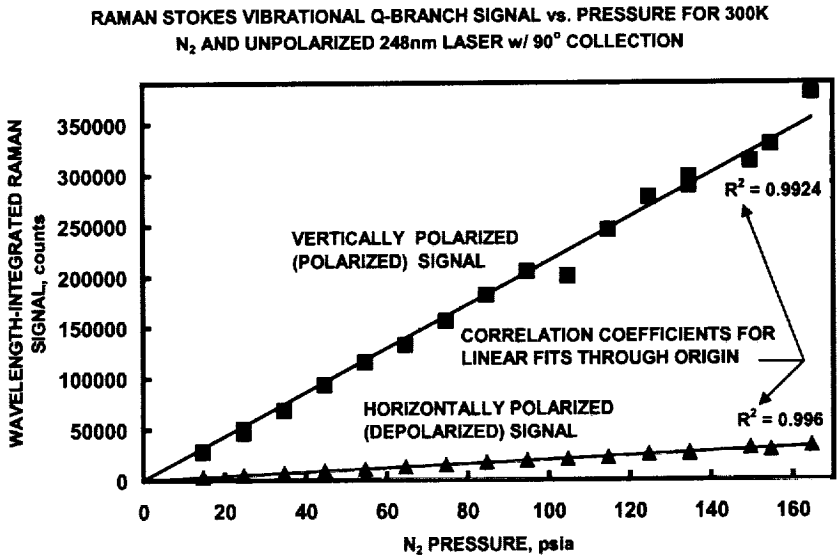

Fig. 12. Polarized Raman signal intensities for N_2 as functions of pressure for N_2 at 300K.

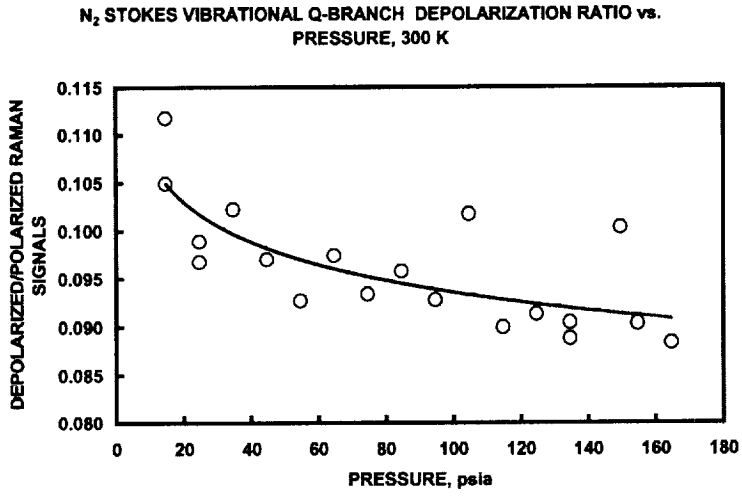

Fig. 13. Depolarization ratio of N_2 at 300K, based on polarized Raman data of Fig. 11.

Calibration

Introduction

Based on the results of the previous section, for pressures from normal atmospheric up to at least 11 atm, the N_2 Raman cross section (for $N_{,,}$ signals) is independent of density. If one assumes that this can be applied to other gas species as well, and to other gas mixtures than for pure N_2, then for each gas species i, the Raman cross section for that species, σ_i, depends upon temperature, T, only, i.e:

$$\sigma_i = \sigma_i(T). \tag{3}$$

At low densities, T influences σ_i because of the variation in ro-vibrational energy level populations and the fact that a molecule's tendency to undergo a Raman scattering event depends on that molecule's ro-vibrational energy level. Though there is a slight dependency on the rotational energy level, J, the more important relationship is for the vibrational quantum number, V. The cross section for a particular vibrational level is related to V by [Long 1977]:

$$\sigma_i(V) \propto (V+1) \tag{4}$$

Integrating over all vibrational energy levels shows that the Raman scattering cross section for a population of molecules for gas species i can be related to temperature through the vibrational partition function Q_v:

$$\sigma_i(T) = (\sigma_{i(300\ K)})(Q_V) \tag{5}$$

where Q_V is given by:

$$Q_V = \left(1 - e^{\left(-T_V/T\right)}\right)^{-1}. \tag{6}$$

In Eq. 6 T_V is the characteristic vibrational temperature, which is a constant for a particular species i. For O_2 T_v is 2274K; for N_2 3392K; and for H_2, 6338K. These T_v values, at T=2000K, produce Q_v values of 1.7, 1.2, and 1.04, respectively. Thus Eqs. 5 and 6 show a simple monotonic increase in Raman cross section with an increase in temperature, with the most increase for O_2 and the least for H_2.

The detected Raman signal depends upon temperature in a second way in addition to distribution of molecules in vibrational levels. The wavelength extents of a particular specie's Raman signal increase with temperature. Figure 14 shows this trend for the Raman spectra of H_2O and H_2 for several different rich H_2-air flames of varying equivalence ratio and stoichiometry. If the light detector is a CCD camera, the entire wavelength range of the Raman signal can be collected, but still the amount that is actually used in a data reduction scheme may be chosen to be less than the total due to overlap of adjacent Raman signals or background interference that may be strong compared to low intensity wavelength regions of a Raman signal

spectrum. If for some reason the entire wavelength range of the Raman spectrum is not collected and used in a subsequent data reduction scheme, then as T increases an increasing percentage of the Raman signal remain undetected (or at least uncollected for use in data reduction). This results in the opposite trend as that shown in Eqs. 5 and 6, and can be represented in Eq. 1 by showing light collection efficiency Ω as a function of T, or $\Omega(T)$. Coupled together these two trends can cancel each other, with then essentially no temperature dependence resulting for the Raman signal, or one process or the other may dominate and each could be the more important process only for a certain temperature range. Thus a calibration is necessary to allow the Raman signals to be transformed into number density (or concentration) measurements.

Calibration Procedure

Keeping in mind that the application of the UV Raman system at Test Stand 115 is for rocket engine-related combustion analysis, where H_2 or hydrocarbons (methane, kerosene, etc.) may be used as the fuels along with LOx used as the oxidizer, the following calibration procedure will provide the detected Raman signal/temperature relationships for the reactants O_2 and H_2, and for the combustion products CO_2, CO, and H_2O. For hydrocarbon reactants such as CH_4 and kerosene, there is no need to determine their Raman signal/temperature relationship because at a relatively low temperature (~500 K) they pyrolize into other gas species such as CH_3 and CH_2.

Referring to Eq. 1, the number density of species i is related to measured Raman signal N_i by:

$$n_i = N_i/(\sigma_i(T)\, N_{laser}\, \Omega(T)\, L) \tag{7}$$

Equation 7 now shows the system's light collection efficiency as a function of temperature. The influence of temperature upon σ_i and Ω can be grouped into one temperature-dependent function, $1/f(T)$, which can have an arbitrarily assigned value of 1.0 at some temperature (typically ~300K). The values for σ_i and Ω can then be assumed constant at their values at 300K. Thus:

$$n_i = (N_i\, f_i(T))/(\sigma_i\, N_{laser}\, \Omega\, L). \tag{8}$$

Assuming that, for a particular experimental configuration, Ω and L do not change, then they can be grouped together into a temperature-independent constant, $1/K_i$ to form the following working equation that relates n_i to N_i:

$$n_i = (N_i\, f_i(T)\, K_i)/N_{laser}\,. \tag{9}$$

The usage of Eq. 8 in actual practice involves obtaining a numerical value of K_i via a known 300K calibration flow, and through a separate calibration determine the $f_i(T)$ to T relationship. Since K_i is is so situational-specific, e.g. depending upon light collection lenses, their focal length, spectrograph used, camera gain, CCD efficiency, etc., its value must be determined at Test Stand 115 and preferably just before or after the UV Raman system is applied to a test article. However $f_i(T)$ can be determined beforehand. The following section shows the results of this calibration.

Choice of Calibration Flames

The calibration system at Vanderbilt follows the schematic of Fig. 9 except that the high pressure cell is replaced by a Hencken multi-element adiabatic diffusion burner. The burner surface is 0.5 inches in diameter and is surrounded by an a 0.25 inch annular co-flow of N_2. By mixing the fuel and oxidizer downstream of the burner face, the burner produces essentially adiabatic flames and requires no water cooling. This enables prediction of post combustion gas mixture concentrations and temperatures by measuring the relative amounts of fuel, oxidizer, and diluents into the burner and using an equilibrium gas code, such as STANJAN or EQUIL, to predict the product concentrations and temperature, assuming complete combustion.

Lean O_2-H_2 flames are used to determine $f_{O2}(T)$. To keep the adiabatic flame temperatures below the maximum safe operating temperature of the Hencken burner these O_2-H_2 flames are diluted with flows of CO_2. Table I shows the flowrates used for all calibration flows. In addition a low temperature (300K) flow of pure O_2 is used, along with a 300K mixture of O_2 and CO_2. For the H_2 calibration several rich O_2-H_2-CO_2 flows are used, along with a 300K flow of H_2 and CO_2. For the H_2O calibration both lean and rich O_2-H_2-CO_2 flames can be used, since H_2O is a combustion product for either of these types of flames. However no low temperature calibration is obtained for H_2O, since only pure O_2, H_2, and CO_2 are used as the three reactant flows, with no water vapor contained by any of those three gas flows.

For the CO_2 calibration, both lean and rich flames can be used, as well as low temperature O_2-H_2-CO_2 gas mixtures. However for the rich flames the equilibrium mole fraction of CO_2 in the products is less than in the reactants because of the water-gas shift reaction:

$$CO_2 + H_2 \rightarrow CO + H_2O \qquad (10)$$

The above chemical reaction is also responsible for producing the equilibrium CO that is used in the CO Raman signal calibration. Thus only rich O_2-H_2-CO_2 flames are used for the CO calibration. Originally it was intended to also inject known amounts of CO into cold and hot reacting flows. However a trace contaminant in the CO source causes significant fluorescence interference with the CO Raman signal and precluded the use of this second set of CO calibration flows.

Representative Raman spectra are shown in Figs. 15 through 18 for several flame or room temperature conditions. Figure 15 is the Raman spectrum for a rich (equivalence ratio = 5) O_2-H_2-CO_2 flame and shows the Raman signals for unreacted fuel (H_2), combustion products (H_2O, and CO from the water-gas shift reaction), and diluent (CO_2). In this rich flame each of these four Raman signals are relatively well-separated. There is some overlap between the H_2 and H_2O Raman signals, but it is relatively insignificant and is important only when there is an extremely strong H_2 Raman signal overlapping an extremely weak H_2O Raman signal. A much more important problem associated with the overlap of adjacent Raman signals is for lean O_2-H_2-CO_2 flames, as shown in Fig. 16. For this lean flame there is unreacted O_2, along with the diluent CO_2. Unfortunately their Raman signals lie so closely together that they significantly overlap. In addition, for lean flames, there can significant fluorescence of vibrationally-excited

O_2. This phenomenon has been investigated [Wehrmeyer et al. 1992] and can be significantly reduced by using a narrowband tunable excimer laser tuned away from an O_2 fluorescence excitation transition. For the spectrum of Fig. 16, the laser has been intentionally tuned onto an O_2 fluorescence transition to show that three O_2 fluorescence emission bands occur in the spectral range of the Raman signals. One of these O_2 fluorescence bands can interfere with the H_2 Raman signal if hot O_2 and H_2 coexist, and another band interferes with the O_2 Raman signal.

The extent of the CO_2-O_2 overlap is demonstrated in Figs. 17 and 18, which are both for room temperature flows. Figure 17 shows the blended Raman spectra of CO_2 and O_2, (with the mole fraction of CO_2 at 0.22) while Fig. 18 shows only the O_2 Raman signal. The peak of the CO_2 Raman signal is at a lower wavelength than the O_2 peak, so the major difference between Figs. 17 and 18 is the absence of the CO_2 "knee" at the low wavelength side of the O_2 Raman spectrum. The CO_2 signal is usually weak compared to O_2, because the CO_2 mole fraction in never large in reacting flows, and as a result its interference with the O_2 Raman signal is of lesser importance than the interference of the strong O_2 signal into the relatively weak CO_2 signal.

Based on the preceding discussion, the degree of complexity with respect to calibration can be considered as progressing from easiest (H_2, H_2O and CO) through moderate (O_2 requiring narrowband laser) to difficult (CO_2 requiring major O_2 correction).

The results of the calibration procedure are shown in Figs. 19 through 23. In each of these graphs are plotted the results of the experimental calibration, along with error bars, for each data point, that show the uncertainty limits for each particular data point. These uncertainties are dominated by the uncertainties in the concentrations of the reactants for the calibration flows. These concentration uncertainties are due to the uncertainties in the mass flowmeter measurements used to obtain the flowrate measurements listed in Table I. The O_2, H_2, and CO_2 flowrate measurements were all obtained using flowmeters with a maximum input of 100 liters/min and an uncertainty of +/-1 liter/min. The usage of smaller flowmeters, with correspondingly smaller measurement uncertainties will result in smaller uncertainties in the data shown in Figs. 19 through 23.

For H_2 the relationship between f(T) and T is based almost entirely upon the effect of T on Raman cross section, since almost all of the H_2 signal can be collected without interference from H_2O. As a result, the f(T) for H_2 is essentially flat across the temperature range of interest, and dips only slightly at higher temperatures, based upon the relatively large characteristic vibrational temperature for H_2 (6338K). This is shown in Fig. 19. The characteristic vibrational temperature temperature for CO is less (3121K) and as a result its f(T) curve is expected to dip more than for H_2, assuming that all of the CO signal can be collected. Figure 20 shows a more significant drop in the $f_{CO}(T)$ than for $f_{H2}(T)$, as expected. Since H_2O is not a simple diatomic molecule, its vibrational partition function is not described by Eq. 6 but is instead a more complicated function of T, that nevertheless should not increase significantly with a moderate increase in temperature. Thus if the entire H_2O Raman signal is collected, the f(T) for H_2O should drop slightly with an increase in temperature, as do those for H_2 and CO. This is indeed the case, as seen in Fig. 21. For both Figs. 20 and 21, since no room temperature data is available, the f(T) curves are normalized based on the lowest temperature data available, rather than for data at 300K.

For the O_2 calibration both temperature dependent effects described above (the increase in cross section and wavelength range with increase in T) are important. In order to avoid interference of the CO_2 Raman signal onto the measured O_2 Raman signal, not all of the O_2 Raman signal is collected. The low wavelength portion of the O_2 Raman signal is not collected, and as temperature increases an increasing percentage of the O_2 Raman signal falls in this wavelength region. This trend tends to counteract the increase in the O_2 Raman cross section with an increase in temperature and hence it cannot be predicted beforehand what the trend in $f_{O2}(T)$ is with an increase in temperature. Figure 22 shows that $f_{O2}(T)$ initially rises from 300K to ~1500K, but then drops for higher temperatures. However the change in $f_{O2}(T)$ across that temperature range is relatively minor (~+/-10%).

Figure 23 shows the $f_{CO2}(T)$ versus T relationship. The entire CO_2 Raman signal is being collected, but there is a significant correction to be made on the "gross CO_2 Raman signal" before it can be related only to CO_2 concentration, since there is substantial interference by the O_2 Raman signal. The extent of the O_2 Raman interference is related to the strength of the O_2 Raman signal and to temperature, however the temperature influence of the O_2 interference can be convolved into $f_{CO2}(T)$. The factor that is multiplied by the O_2 Raman signal, (N_{O2}) to determine the correction to the gross CO_2 Raman signal ($N_{CO2,\ gross}$), is determined to be 0.182. Thus the net CO_2 Raman signal ($N_{CO2,\ net}$), used to produce Fig. 23, is given by:

$$N_{CO2,\ net} = N_{CO2,\ gross} - (0.182)\ (N_{O2}). \qquad (11)$$

Figure 23 shows a profound influence of T upon $f_{CO2}(T)$. The value of $f_{CO2}(T)$ drops from its normalized value of 1.0 at 300 K down to ~0.3 at 2000K, a drop of over a factor of three. The vibrational partition function for CO_2 is more complicated than that shown in Eq. 6; there are two fundamental vibrational frequencies that are Raman active, rather than just one, and hence at least two characterisitic vibrational temperatures for the two Raman active vibrational modes. One of these two vibrational frequencies has a small characteristic vibrational temperature (960K) and as a result its contribution to the CO_2 vibrational partition function can be expected to vary greatly with temperature. Thus the large difference between $f_{CO2}(T)$ at 300K and at flame temperatures is not surprising. In fact a large change in f(T) has also been seen in visible Raman work performed at Vanderbilt [Cheng 2001]. Table II lists the equations developed that relate $f_i(T)$ to T for the gas species mentioned above.

Temperature Measurement

Each of the $f_i(T)$ described in the previous section has a best-fit curve, together with equations for those curves shown on their respective graphs. These functions (listed in Table II) generally show a nonlinear relationship between $f_i(T)$ and T. They imply that if T is known then $f_i(T)$ values can be determined and hence the various n_i can be found. However often T is not known although the local pressure, P, may be known. If a state relationship can be assumed, such as the perfect gas law corrected by a compressibility factor Z, then the knowledge of P, combined with the various N_i can be used to determine T as well as the n_i. The perfect gas law, including the Z modification, can be written as:

$$P = Z\,n\,k\,T \tag{12}$$

where k is the Boltzmann constant and n is the total number density of molecules. At low pressures Z can be assumed to be unity, but at high pressures Z can deviate significantly from unity, and Z can depend upon P, T, and the gas mixture. Inserting the expression for n_i given by Eq. 9 into Eq. 12, gives:

$$0 = \frac{ZkT}{N_{laser}}\left(\sum_{i=1}^{n} N_i f_i(T) K_i\right) - P \tag{13}$$

Equation 13 shows that an implicit relationship between T and the n_i's. Through an iterative, root-finding numerical procedure, the values of T and n_i can be determined. This iteration may or may not involve Z, depending on whether the pressure and temperature combination require the inclusion of a nonunity Z.

For application to the Test Stand 115 system, the only calibration data that need to be determined are the K_i values. These can be determined for CO_2, O_2, and H_2 by issuing normal temperature (300K) reactants through a Hencken burner or some other small nozzle mounted either in the test article or at the future location of the test article. If the test article is mounted at the location afterward, then a second measurement of ambient O_2 can be used to determine the reduction in Ω_{O2} due to the test article windows and possible aperturing by the test article. An assumption for this process is that every Ω_i will be affected by the same percentage as will Ω_{O2} when the test article is inserted into the optical system. Using the H_2O contained in ambient outdoor air, the value of K_{H2O} can be determined. To determine K_{CO}, a small but known amount of CO can be injected into a flow of ambient temperature CO_2. Finally, if a gaseous hydrocarbon fuel is used, such as CH_4, a small mole fraction of it can be injected into a flow of ambient temperature CO_2. As mentioned previously, it is assume that f(T) for a hydrocarbon fuel remains at unity across the small range of temperature for which the hydrocarbon fuel remains unpyrolized.

Table I. Flowrates used for calibration flows in Hencken burner, together with predicted product temperatures and mole fractions assuming complete reaction and adiabatic equilibrium.

Flowrates, liter/min			Temperature, K	Product Mole Fractions				
O_2	H_2	CO_2		O_2	H_2	CO	CO_2	H_2O
Room Temperature Flows								
9.7	0.0	0.0	300	1.00	0.00	0.00	0.00	0.00
9.7	0.0	2.7	300	0.78	0.00	0.00	0.22	0.00
0.0	20.6	3.0	300	0.00	0.87	0.00	0.13	0.00
Lean Flames								
9.9	1.3	2.8	955	0.69	0.00	0.00	0.21	0.10
9.7	2.7	2.7	1530	0.61	0.00	0.00	0.20	0.20
9.7	5.3	2.6	2258	0.46	0.00	0.00	0.17	0.34
9.7	10.2	2.6	2655	0.25	0.01	0.03	0.16	0.48
Rich Flames								
2.4	20.6	3.0	1608	0.00	0.56	0.11	0.02	0.31
2.9	20.6	3.0	1850	0.00	0.52	0.11	0.02	0.35
3.9	20.6	3.0	2265	0.00	0.43	0.11	0.02	0.44
4.9	20.6	3.0	2562	0.00	0.34	0.10	0.02	0.50

Table II. Temperature dependencies of collected Raman signals.

Gas Species	f(T, in K)
CO_2	$1.25\ e^{(-0.0007\ T)}$
O_2	$(-2.0 \times 10^{-7})\ T^2 + 0.0006\ T + 0.835$
CO	$(-1.0 \times 10^{-7})\ T^2 + 0.0002\ T + 1.0$
H_2O	$(2.0 \times 10^{-8})\ T^2 - 0.0002\ T + 1.2$
H_2	$(-4.0 \times 10^{-8})\ T^2 + (8.0 \times 10^{-5})\ T + 1.0$

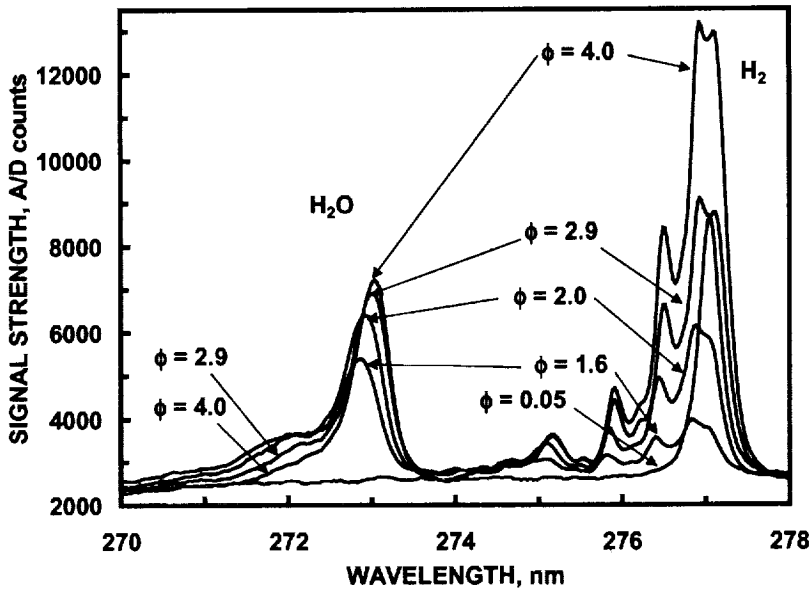

Fig. 14. Raman spectra of H_2 and H_2O at different flame temperatures for rich H_2-air flames of several equivalence ratios (ϕ).

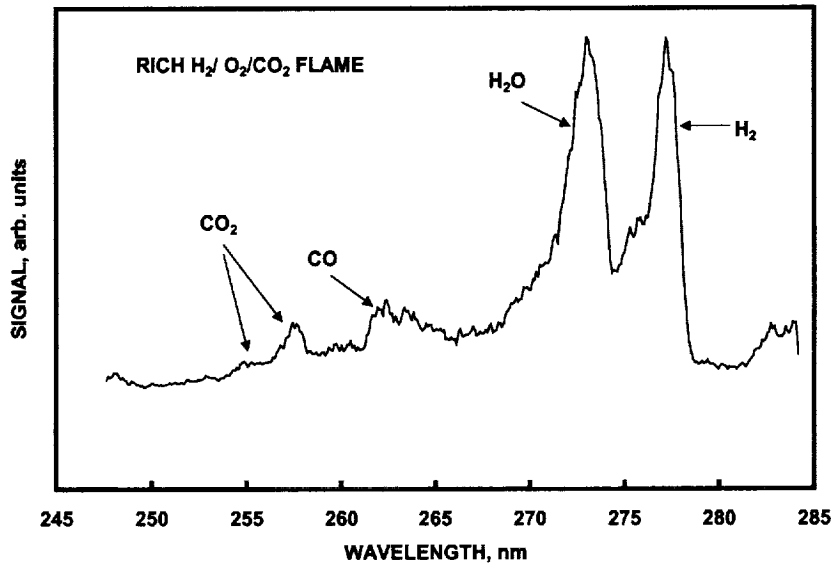

Fig. 15. UV Raman spectra in rich O_2-H_2-CO_2 flame showing CO_2, CO, H_2O and H_2 Raman signals.

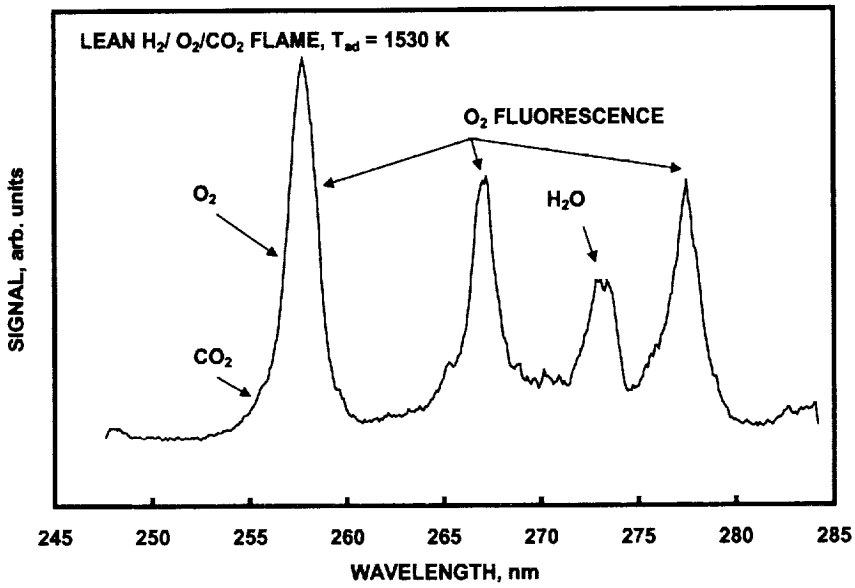

Fig. 16. UV Raman spectra in lean O_2-H_2-CO_2 flame showing CO_2, O_2, and H_2O Raman signals together with O_2 fluorescence.

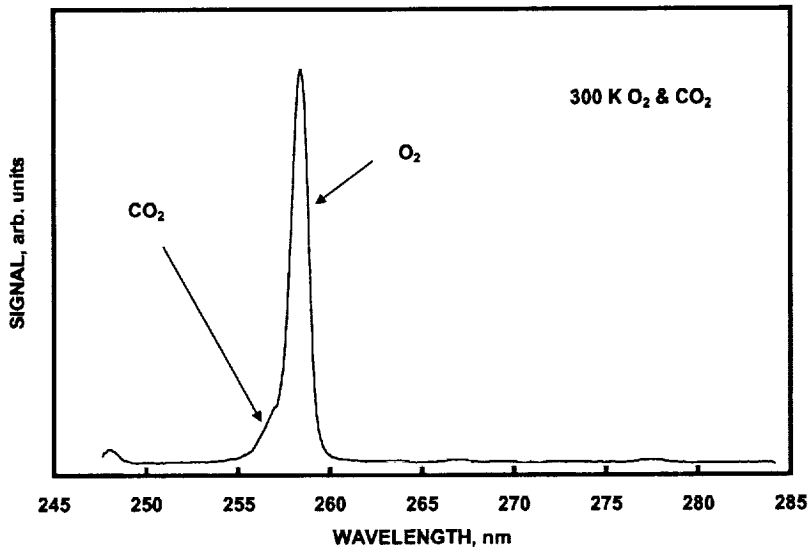

Fig. 17. UV Raman spectrum of a mixture of room temperature CO_2 and O_2. Mole fraction of CO_2 at 0.22.

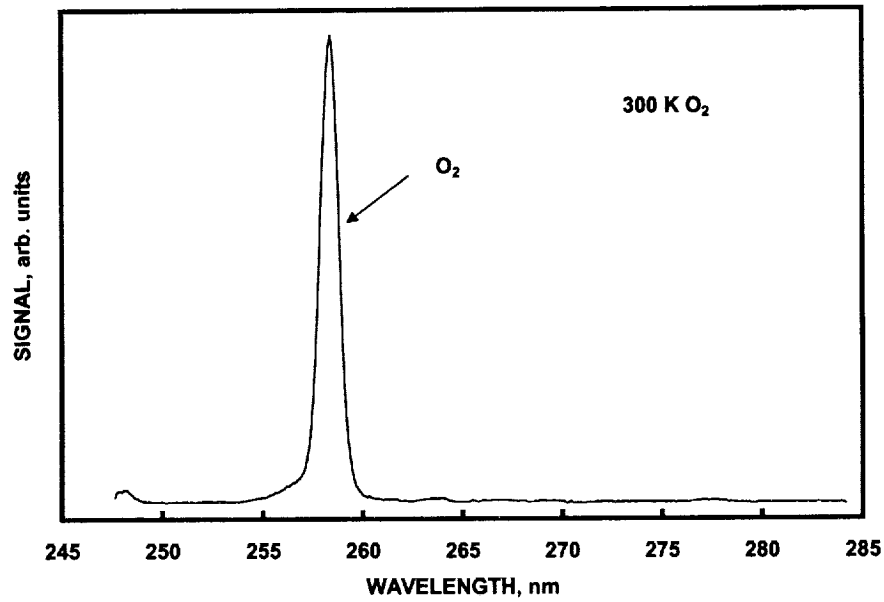

Fig. 18. UV Raman spectrum of pure O_2.

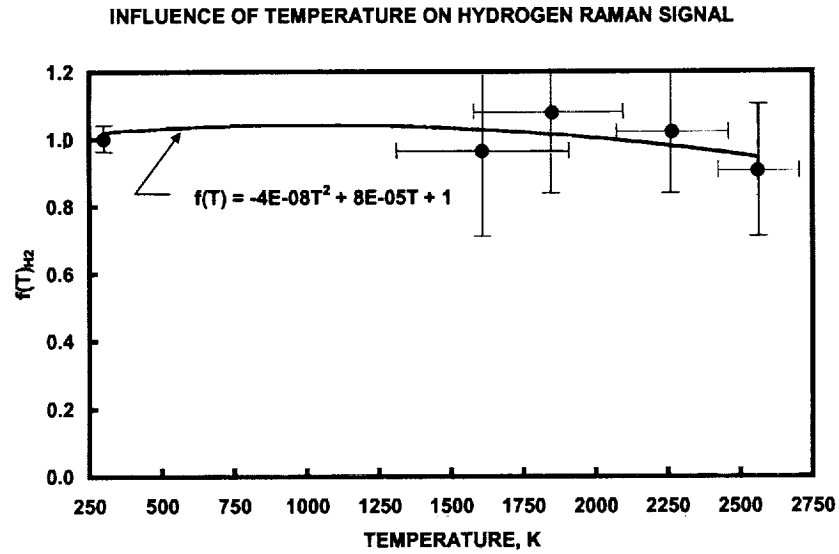

Fig. 19. Relationship between f(T) and T for H_2.

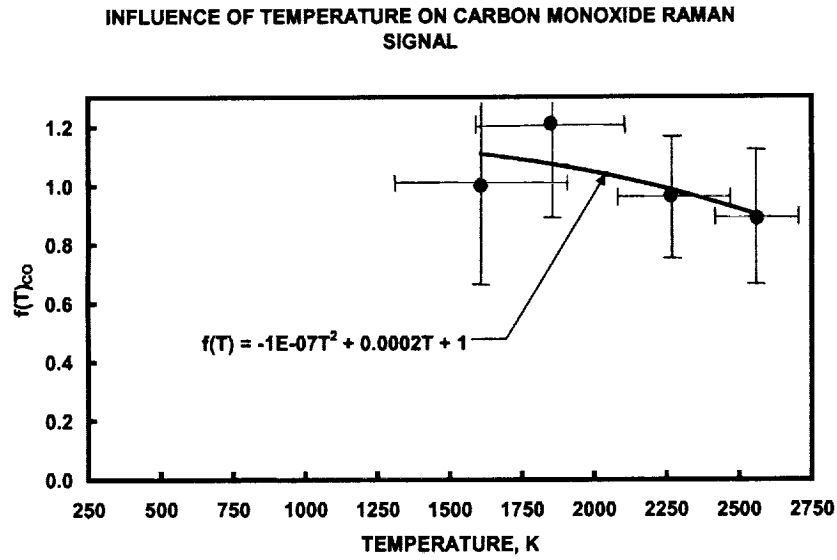

Fig. 20. Relationship between f(T) and T for CO.

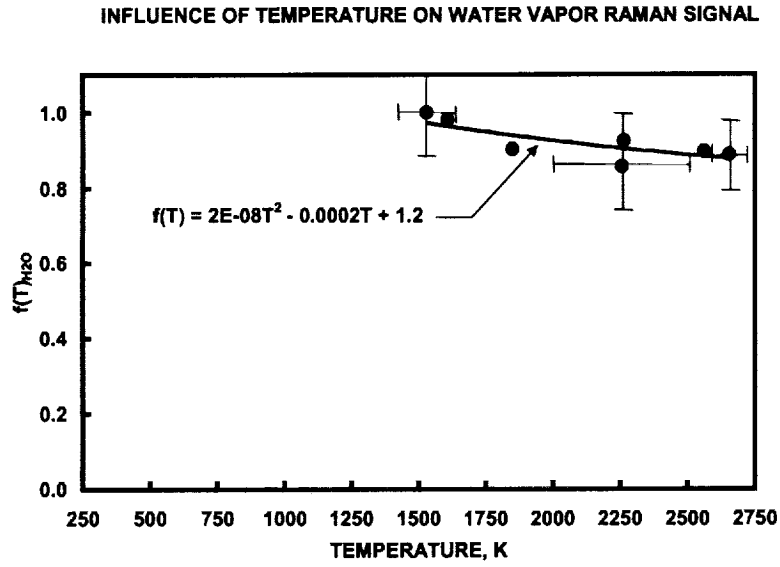

Fig. 21. Relationship between f(T) and T for H_2O.

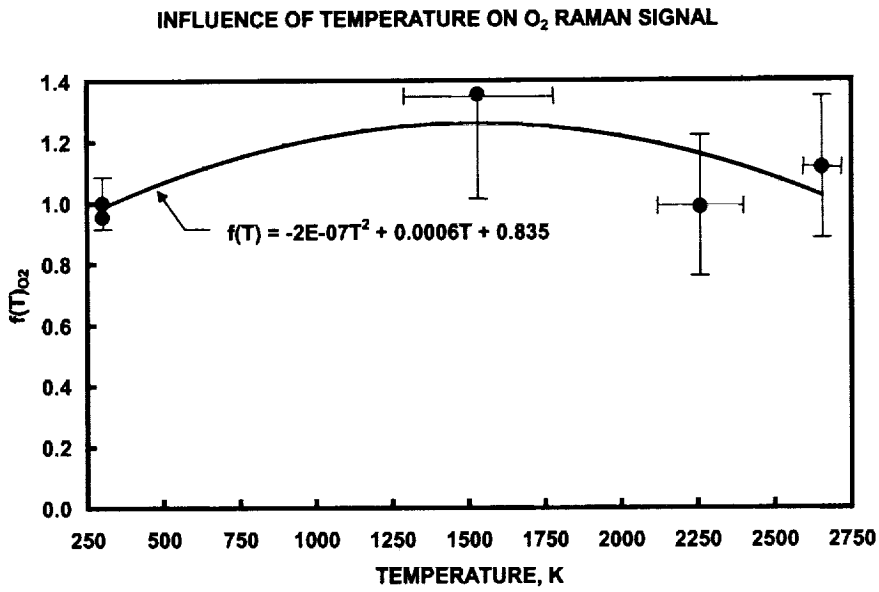

Fig. 22. Relationship between f(T) and T for O_2.

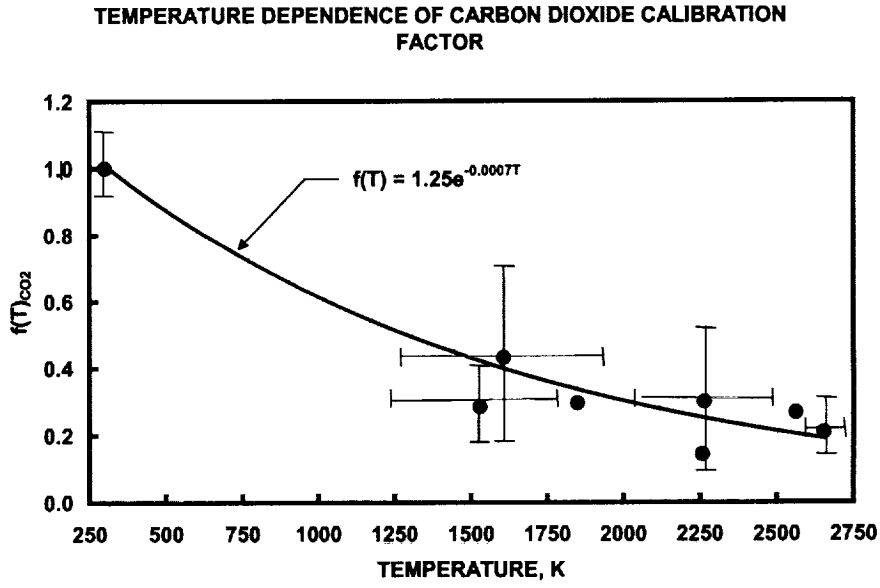

Fig. 23. Relationship between f(T) and T for CO_2.

High Spectral Resolution UV Raman for Temperature Measurement

Some applications of the UV Raman system will be to flows for which the local pressure cannot be measured, such as in supersonic exhaust flows where shocks and expansion fans delineate regions of disparate static pressure. For these applications a modification to the current single-pulse UV Raman system at Test Stand 115 has been implemented. This modification involves using a small entrance slit aperture for the imaging spectrograph, and as a result fine spectral resolution is obtained at the expense of signal strength reduction. The loss of signal strength makes this technique a time-averaged one, requiring the accumulation of signal from several laser pulses, but the good spectral resolution allows structural details of the Raman signal to become discernable and these can be related to temperature. As an example, the spectral shape of the the H_2 Raman signal is shown in Fig. 24 for a rich H_2-air flame produced in a Hencken burner. This experimental spectrum is compared to several theoretically predicted spectra, and the temperature associated with the best-fitting theoretical spectrum (2400K) taken as the temperature for the flame. Details of this time-average temperature measurement technique using spectrally-resolved UV Raman can be found in Wehrmeyer et al. (2001b).

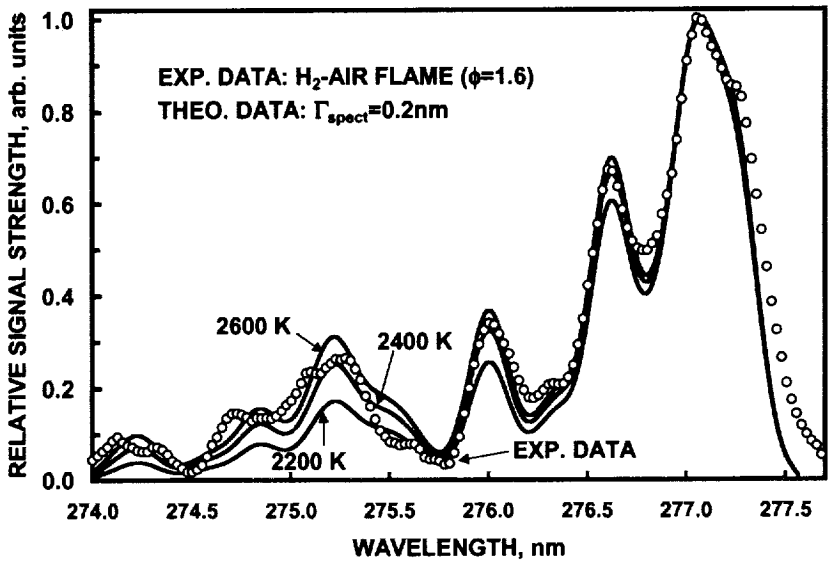

Fig. 24. Theoretical and experimental high resolution UV Raman spectra of rich H_2-air flame.

Summary, Conclusions, and Future Work

An investigation into the effect of high pressure upon the signal strength and polarization properties of UV Raman signals has performed. Due to safety limitations only pressures up to 165 psia (11 atm) were experimentally investigated. Examining the UV Raman signal strength for N_2 at 300K, a simple linear relationship between pressure and signal strength was measured, indicating no enhancement of the N_2 cross section with an increase in pressure up to 11 atm. A small drop (~10%) in the depolarization ratio for N_2 was detected, and is consistent with the work of others [Wang and Wright 1973]. Their work extended to higher pressures as did the work of Fabre and Oksengorn [1992] and showed that at the highest pressures associated with rocket engine combustion (~3000psia) there can be a significant (~25%) increase in Raman cross sections, although the signals retain their polarized nature.

The 11 atm experimental work of this effort, together with others' previous works, show that no increase in depolarization in the UV Raman signal is expected for an increase in pressure. In fact the opposite trend is expected: the Raman signal is expected to become even more polarized at high pressures, at least for N_2. Thus the high pressure polarized UV Raman images shown in Fig. 7, that show Raman signals of approximately equal signal strength for both polarizations, cannot be explained by the effect of gas pressure on polarization properties. The fused silica windows were also examined under high pressure (165 psia) to determine if they have pressure- (or stress-) dependent polarization properties. No effect was seen on the polarized transmission characteristics of the fused silica windows. There has been an investigation, at DLR, into the effect of stress-induced birefringence in fused silica windows at high pressures. This German investigation has detected some influence of pressure on the window polarization properties [Meier et al. 2001]. Window thickness must be related to the extent of this polarization effect. The DLR windows could be thinner than the thick MCTA windows and as a result could have more of a pressure effect. As a future effort, an investigation into the polarization properties of fused silica windows of varying thickness and diameter should be performed, at pressures associated with realistic rocket engine combustion. This will probably require use of the MCTA and ancillary high pressure facilities that are available at Test Stand 115.

A calibration procedure, using several flows of lean or rich O_2-H_2-CO_2 gas mixtures, was developed at Vanderbilt. As a result of the calibration the temperature dependencies of the detected Raman signals have been determined. These results are given in Table II. Along with these $f_i(T)$ values, a factor of 0.182 was also determined for the multiplier to be applied to the O_2 Raman signal to determine the amount of O_2 interference to be subtracted from the CO_2 signal. These data can be used, along with K_i values determined in the field since they are so situational-specific, to transform qualitative Raman data into quantitative temperature and gas concentration measurements, assuming that independent pressure measurements are available together with the Raman data.

With a slight modification (narrowing the entrance slit) of the spectrograph the UV Raman system at Test Stand 115 can be used to provide temperature measurements in flows where local pressure is not known. A further improvement to the UV Raman system would be the simultaneous use of two spectrographs, one with a wide slit used to obtain single pulse data

with which to determine qualitative information about the mixing and reaction state of a flow at an unkown pressure, and a second spectrograph with narrow slit used to obtain time-averaged temperature measurements.

References

Cheng, Zhongxian. 2001. "Visible Laser Raman Diagnostics Application in Partially Premixed Flames of Premixed Fuel Versus Hot Products." Masters Thesis, Mechanical Engineering Department, Vanderbilt University.

Fabre, D., and B. Oksengorn. 1992. "Pressure and Density Dependence of CH_4 and N_2 Raman Lines in an Equi-Molar CH_4/N_2 Gas Mixture." *Applied Spectroscopy* 46: 468-471.

Gu, Y., Y. Zhou , H. Tang , E.W. Rothe , G.P. Reck. 2000. "Pressure Dependence of Vibrational Raman Scattering of Narrow-Band, 248-nm, Laser Light by H_2, N_2, O_2, CO_2, CH_4, C_2H_6, and C_3H_8 as high as 97 bar." *Applied Physics B: Laser and Optics* 71: 865-871.

Hartfield, R., C. Dobson, R. Eskridge, and J. Wehrmeyer. 1997. "Development of a Technique for Separating Raman Scattering Signals from Background Emission with Single-Shot Measurement Potential. " AIAA Paper 97-3357 presented at the 33rd Joint Propulsion Conference, Seattle, WA, July 6-9

Lapp, M., C. M. Penney, and J. A. Asher. 1973. "Application of Light-Scattering Techniques for Measurements of Density, Temperature, and Velocity in Gasdynamics." Air Force Report ARL 73-0045, submitted by General Electric Company for Contract F33615-71-C-1867.

Long, D. A., 1977. "*Raman Spectroscopy.*" McGraw-Hill: New York.

Meier, W., O. Keck, J. Hussong, and W. Stricker. 2001. "Laser Raman Scattering Applied in Technical Combustors: Strategies and Limitations." Poster presented at the Gordon Research Conference on Laser Diagnostics in Combustion, Mount Holyoke College, South Hadley, MA.

Wang, C. H., and R. B. Wright. 1973. "Effect of Density on the Raman Scattering of Molecular Fluids. I. A Deatiled Study of the Scattering Polarization, Intensity, Frequency Shift, and Spectral Shape in Gaseous N_2." *Journal of Chemical Physics* 59: 1706-1712.

Wehrmeyer, J. A., J. M. Cramer, R. H. Eskridge, and C. C. Dobson. 2001a. "Ultraviolet Raman Diagnostics for Rocket Engine Injector Development."*Journal of Propusion. and Power* 17: 27-34.

Wehrmeyer, J. A., R. J. Osborne, and H. P Trinh. 2001b. "Measuring Rocket Engine Temperatures With Hydrogen Raman Spectroscopy." Paper presented at the Penn State Propulsion Engineering Research Center's 13th Annual Symposium on Propulsion, Huntsville, AL, Oct. 22-23.

Wehrmeyer, J. A., H. Trinh, R. Hartfield, C. Dobson, and R. Eskridge. 2000. "Raman Gas Species Measurements in Hydrocarbon-Fueled Rocket Engine Injector Flows." AIAA Paper 2000-3391 presented at the 36th AIAA Joint Propulsion Conference, Huntsville, AL, July 17-19.

Wehrmeyer, J. A., J. Cramer, R. Eskridge, and C. Dobson. 1997. "UV Raman Diagnostics for High Pressure Rocket Engine Injector Flowfields. " AIAA Paper 97-3357 presented at the 33rd AIAA Joint Propulsion Conference, Seattle, WA, July 6-9.

Wehrmeyer, J. A., T. S. Cheng, and R. W. Pitz. 1992. "Raman Scattering Measurements in Flames Using a Tunable KrF Excimer Laser." *Applied Optics* 31: 1495-1504.